JACS
JOURNAL OF THE AMERICAN CHEMICAL SOCIETY
Communication
pubs.acs.org/JACS

Metallic Iron–Nickel Sulfide Ultrathin Nanosheets As a Highly Active Electrocatalyst for Hydrogen Evolution Reaction in Acidic Media

Xia Long,[†] Guixia Li,[‡] Zilong Wang,[†] HouYu Zhu,[‡] Teng Zhang,[†] Shuang Xiao,[†] Wenyue Guo,[‡] and Shihe Yang*[,†]

[†]Department of Chemistry, William Mong Institute of Nano Science and Technology, The Hong Kong University of Science and Technology, Clear Water Bay, Kowloon, Hong Kong

[‡]College of Science, China University of Petroleum, Qingdao 266555, PR China

Supporting Information

ABSTRACT: We report on the synthesis of iron-nickel sulfide (INS) ultrathin nanosheets by topotactic conversion from a hydroxide precursor. The INS nanosheets exhibit excellent activity and stability in strong acidic solutions as a hydrogen evolution reaction (HER) catalyst, lending an attractive alternative to the Pt catalyst. The metallic α-INS nanosheets show an even lower overpotential of 105 mV at 10 mA/cm^2 and a smaller Tafel slope of 40 mV/dec. With the help of DFT calculations, the high specific surface area, facile ion transport and charge transfer, abundant electrochemical active sites, suitable H^+ adsorption, and H_2 formation kinetics and energetics are proposed to contribute to the high activity of the INS ultrathin nanosheets toward HER.

The growing demand for energy and environmental concerns have stimulated global efforts to explore alternative energy sources to fossil fuels. As an ideal candidate, hydrogen produced from water splitting is especially attractive.[1] The Pt group metals are most active in catalyzing the hydrogen evolution reaction (HER), but the high cost and elemental scarcity greatly hinder their widespread applications.[2]

Recently, transition metal dichalcogenides (TMD), WS_2, MoS_2, $MoSe_2$, etc., have been surveyed as HER catalysts because of the low cost and high stability on top of the general interest in two-dimensional (2D) materials.[3] Surprisingly, nickel sulfides, NiS, NiS_2, Ni_3S_4, etc., have rarely been studied as HER catalysts despite their extensive use as electrode materials for supercapacitors and Li-ion batteries.[4] Insomuch as Fe impurity could greatly improve the oxygen evolution reaction (OER) performance of nickel hydroxide/oxide by changing the local electronic structure,[5] it is reasonable to expect a similar influence of Fe on the HER catalytic activity of nickel sulfides. Herein, we show that with Fe incorporation, both the HER catalytic activity and stability of nickel sulfide (iron–nickel sulfide, INS) ultrathin nanosheets are greatly improved, outperforming most of the known transition metal based HER catalysts in acidic solutions. In particular, the INS nanosheets put at a disadvantage the more widely investigated TMD electrocatalysts, such as MoS_2 and WS_2,[3a−f,6] which exhibit good HER performance only after transformation from the thermodynamically favored 2H phase to the 1T polymorph.[3b,f,6c] By annealing treatment, we obtained metallic α-INS nanosheets, which showed further improved HER performance. In conjunction with theoretical calculations, we have studied the origins of the advanced catalytic properties.

The β-INS ultrathin nanosheets were synthesized by a topotactic conversion reaction, starting from FeNi layered double hydroxide (LDH) nanosheets (Figures 1A and S1).[7]

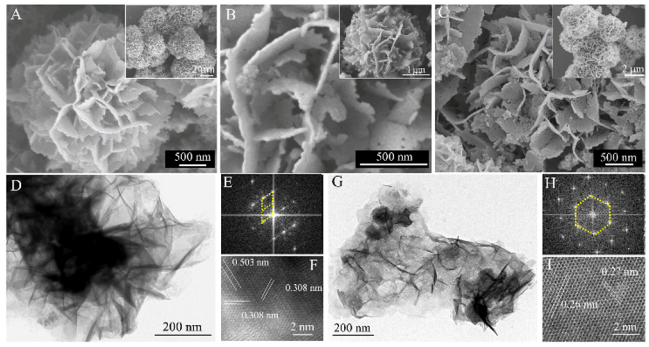

Figure 1. Morphology and structure characterizations. SEM images of (A) FeNi LDH precursor, (B) β-INS nanosheets, and (C) metallic α-INS nanosheets. TEM images (D, G), HRTEM images (F, I) and the corresponding Fourier transformed patterns (E, H) of the β-INS (D, E, F) and the α-INS (G, H, I) nanosheets. The Fourier transformed patterns (E, H) are rhombohedral and hexagonal, respectively, for the β-INS and α-INS nanosheets.

Scanning electron microscopy (SEM) (Figure 1B) and transmission electron microscopy (TEM) (Figure 1D) images indicate that the nanosheet morphology of the LDH precursor with a lateral size of several micrometers was well preserved after the sulfidation treatment. The corresponding energy dispersive X-ray (EDX) elemental mapping images in Figure S2 verify the existence of Fe, Ni, and S and show a uniform distribution of these elements with an Fe/Ni atomic ratio of ~1/10, consistent with the XPS result (Table S1). The high resolution TEM (HRTEM) image in Figure 1F shows lattice fringes of (300), (101), and (110) planes, which correspond to d = 0.308, 0.325, and 0.503 nm, respectively, slightly larger than those of rhombohedral β-NiS due to the substitution of Fe for Ni.

Received: July 23, 2015
Published: September 4, 2015

DOI: 10.1021/jacs.5b07728
J. Am. Chem. Soc. 2015, 137, 11900−11903

From the atomic force microscopic (AFM) height images, the thickness of the β-INS nanosheet was measured to be around 2 nm (Figure S3A,B), a little larger than that of the LDH precursor (Figure S3C,D). In contrast to the smooth surfaces of the FeNi LDH nanosheet precursor (Figure S1), the β-INS nanosheets are porous with rough surfaces (Figure 1B), indicating the successful transformation from LDH to β-INS.

The X-ray diffraction (XRD) patterns of the LDH precursor and the β-INS nanosheets are shown in Figure S4A. The diffraction peaks of the LDH precursor are ascribed to (003), (006), and (012) planes of β-Ni(OH)$_2$, positively shifted due to the substitution of Fe for Ni.[7,8] After sulfidation, the β-INS nanosheets show diffraction peaks of (110), (101), and (300) planes of rhombohedral NiS with similar positive shifts, which are consistent with the HRTEM result (Figure 1F) and thus confirm the successful conversion of FeNi LDH to β-INS.

X-ray photoelectron spectroscopy (XPS) showed the existence of Fe, Ni, and S in β-INS ultrathin nanosheets (Figure S4B). The Ni 2p XPS spectrum was best fitted with one spin−orbit doublet (Figure S5), which is characteristic of Ni^{2+} (magenta curves) and two shakeup satellites (blue curves).[9] The Fe 2p high resolution XPS spectrum is deconvoluted into four peaks: two fitted in the Fe 2p$_{1/2}$ region and two in the Fe 2p$_{3/2}$ region, which could be explained by the coexistence of Fe^{2+} (magenta curves) and Fe^{3+} (blue curves).[10] The activity of HER catalyst was reported to be sensitive to the valence state and coordination environment of the metal centers.[11] From the deconvoluted XPS peaks of metal ions, both the Ni and Fe peaks are positively shifted, suggesting strong interactions involving the ions.[12] This may have important implications in modulating electronic environments of the metal centers in β-INS ultrathin nanosheets and thus promoting the HER catalysis.

For the electrochemical characterizations in 0.5 M H_2SO_4, Ag/AgCl and platinum (Pt) wire were used as reference and counter electrode, respectively. β-INS catalyst coated on glass carbon (GC) was applied as working electrode. Figure 2A shows the polarization curves of catalyzed HER. As expected, Pt wire showed a superior HER activity with a negligible overpotential (Figure 2A, black curves), whereas bare GC showed no HER activity with a negligible current density even at −0.3 V vs RHE (Figure 2A, purple curves). The β-NiS nanosheets (Figure S6A,B) exhibited a moderate HER activity with an overpotential of 202 mV at 10 mA/cm^2 (magenta curves), but the β-INS nanosheets showed a much lower overpotential of 117 mV at 10 mA/cm^2 (Figure 2A, blue curves), in fact lower than most non-noble-metal based HER catalysts reported so far (Table S2). We believe that the high HER activity stems from the rich redox reaction centers of ultrathin nanosheets as well as synergetic effects of the bitransition metals.[13]

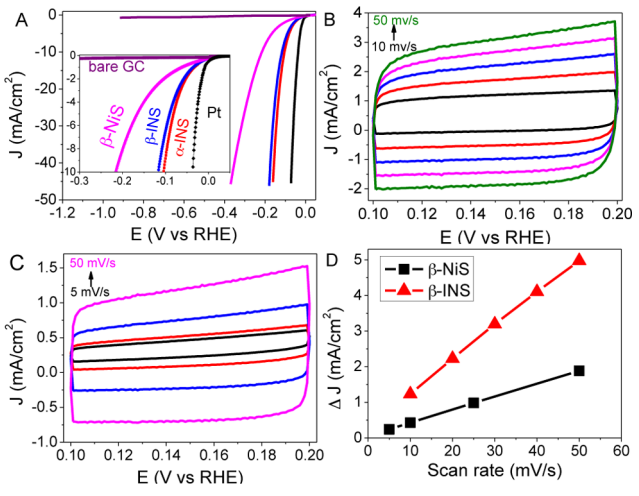

Figure 2. Electrochemical performance and electrochemical surface area (ECSA) tests of catalysts toward HER in the acidic electrolytes of 0.5 M H_2SO_4. (A) Linear sweep voltammetry (LSV) curves of β-NiS, β-INS, and α-INS catalyzed HER, (B) CV curves of β-INS and (C) β-NiS nanosheets with various scan rates. (D) Charging current density differences plotted against scan rates. The linear slope, equivalent to twice the double-layer capacitance, C_{dl}, was used to represent the ECSA.

High surface area is requisite for an advanced electrocatalyst. For the β-INS ultrathin nanosheets, the nitrogen adsorption−desorption isotherm (Figure S7A) measured a Brunauer−Emmett−Teller (BET) surface area at 109.83 m^2/g, much higher than that of FeNi LDH precursor (54.68 m^2/g, Figure S7B) and β-NiS nanosheets (80.44 m^2/g, Figure S7C). We further tested the electrochemical double layer capacitances (C_{dl}) of the catalysts by a simple cyclic voltammetry method[6c,14] (Figure 2B,C) to relate the catalytic activity with the electrochemical surface area (ECSA). From Figure 2D, it is clear that the C_{dl} of β-INS at 46.4 μF is about three times higher than that of β-NiS (15.5 μF). The increase of ECSA is attributed to the enhanced anion exchangeability between the electrolyte and catalytic active sites. In return, the increased catalytic active sites and enhanced anion accessibility enabled by the porous nanosheet structure resulted in the significant improvement of catalytic performance (*vide infra*).

In order to further improve the HER kinetics, the rhombohedral β-INS nanosheets were annealed in an Ar atmosphere at 450 °C for 5 h and transformed to hexagonal α-INS, which have metallic properties. From the XRD peaks of α-INS (Figure S4A, blue curve), the d spacings are calculated to be 2.99, 2.71, 2.63, and 2.02 nm, which are consistent with the HRTEM observation (Figure 1I) and can be ascribed to (100), (002), (101), and (102) planes of α-NiS, respectively, thereby confirming the successful transformation of β-INS to α-INS. The as transformed α-INS still kept the nanosheet structure of β-INS on comparing the SEM (Figure 1C) and TEM (Figure 1F) images. Next, the resistivities of β-INS and α-INS were measured at room temperature to be 1.18 × 10^{-3} Ω·cm and 5.15 × 10^{-5} Ω·cm, respectively, differing by as much as about 2 orders of magnitude. Plausibly, the α-INS behaves as a metal (~10^{-5} Ω·cm). Advantageously, the intrinsic metallic character of the α-INS nanosheets contributes to the HER catalysis. First, the intrinsic high conductivity allows it to supply charges on demand to sustain and facilitate the HER process. Second, it ensures an ohmic contact at the catalyst−GC electrode and catalyst−electrolyte interfaces for fast charge transfer since no additional overpotential is needed to overcome the Schottky barrier[15] commonly encountered in HER electrocatalysis. Indeed, from the LSV curve of α-INS catalyzed HER (Figure 2A, red curves), it is clear that the potential needed to achieve the current density of 10 mA/cm^2 is positively shifted from −117 mV for β-INS to −105 mV for α-INS, confirming the higher HER activity of α-INS than β-INS nanosheets. It is noteworthy that the electrochemical performance of metallic α-NiS is also enhanced (Figure S8). The overpotential needed to achieve a specific current density was further decreased in our favor with increasing *iR* compensation level (Figure S9A). Of

DOI: 10.1021/jacs.5b07728
J. Am. Chem. Soc. 2015, 137, 11900−11903

note, the LSV curves for α-INS nanosheets by using Pt (black curve) and graphite rod (red curve) as the counter electrode are quite similar, except for only a slightly increased overpotential that is required to achieve the same current density for the latter (Figure S9B), indicating that the high HER performance of α-INS nanosheets indeed reflects the intrinsic high catalytic activity of α-INS nanosheets instead of Pt contamination.

The Tafel slope was determined to evaluate HER kinetics. As shown in Figure 3A, the measured Tafel slope for Pt is about 33

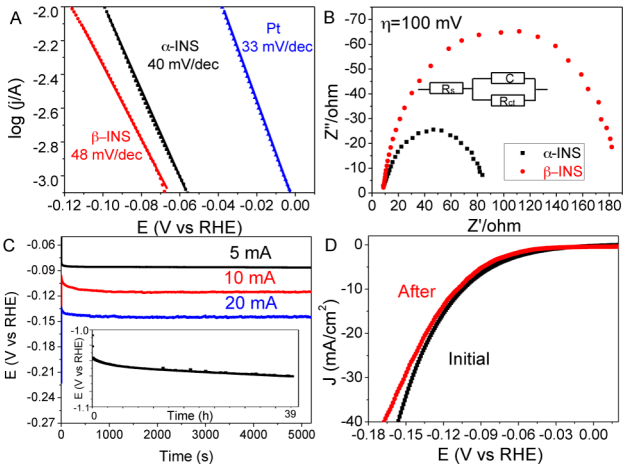

Figure 3. (A) Tafel plots of Pt, β-INS, and α-INS catalyzed HER, (B) electrochemical impedance spectra (EIS) of β-INS and α-INS nanosheet catalyzed HER at overpotential of 100 mV, (C) chronopotentiometry test of α-INS at the current density of 5, 10, and 50 mA/cm^2 (inset, long time CP testing of α-INS at the current density of 10 mA/cm^2), and (D) LSV curves of α-INS nanosheets on HER before and after the CP testing at 10 mA/cm^2 for nearly 40 h.

mV/dec, close to the literature values.[16] The Tafel slope of β-INS is around 48 mV/dec, which is further decreased to 40 mV/dec for α-INS. As far as we know, this value is the smallest one to date for nickel sulfide based HER catalysts and comparable to or even smaller than that of many Mo- and W-based HER catalysts shown in Table S2. The low Tafel slope of 40 mV/dec is indicative of the Volmer–Heyrovsky mechanism,[17] which comprises fast discharge of a proton and a slow combination of the discharged proton with an additional proton [$H_{ad} + H_3O^+ + e^- \rightarrow H_2 + H_2O$]. The fast electrode reaction kinetics of α-INS is made more evident by electrochemical impedance spectroscopy (EIS). Figure 3B shows the Nyquist plots of α-INS (black curve) and β-INS (red curve) nanosheets at the overpotential of 100 mV. The EIS data reveals a much smaller charge transfer resistance (R_{ct}, 63.16 Ω) of the α-INS electrode than that of β-INS (154.5 Ω), suggesting a much faster electron transfer and a higher Faradaic efficiency during HER. This benefits from the unique electronic properties and the ohmic contact of the α-INS nanosheets. Moreover, the BET specific surface area of α-INS is close to that of β-INS nanosheets (Figure S10), while the C_{dl} of α-INS (56.23 mF, Figure S11) is larger than that of the β-INS catalyst, reflecting a relatively larger ECSA associated with more exposed catalytic active sites for the α-INS nanosheets, leading to a larger exchange current density of α-INS than that of β-INS (Figure S12).

Yet another important criterion for an HER catalyst is its operational stability. For this purpose, we chose α-INS nanosheet and tested it by chronopotentiometry (Figure 3C). The potential needed to achieve the high current densities (5 mA/cm^2, 10 mA/cm^2 and 20 mA/cm^2) were negligibly declined over the 3500 second and decreased slightly even for 40 h (Figure 4C inset). Moreover, after the chronopotentiometry test, the polarization curve showed a very small negative shift (Figure 3D, red curve) compared with the initial one (Figure 4D, black curve). These results suggest the long-term superior stability of the α-INS ultrathin toward HER.

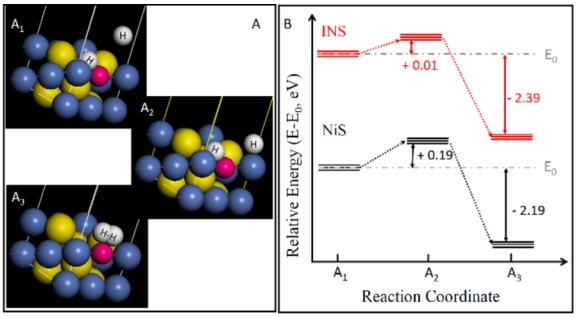

Figure 4. (A) Schematic reaction pathway of HER on α-INS ultrathin nanosheets in acid environment. (B) Kinetic energy barrier profiles of HER on α-INS and α-NiS nanosheets. The yellow, blue and red spheres in A_1–A_3 represent S, Ni, and Fe atoms, respectively.

To understand the catalytic efficacies arising from the Fe incorporation, the detailed HER pathways on both the α-NiS and α-INS catalysts were investigated by DFT calculations (Figure 4; also see SI for details). In the DFT calculation, a proton was first adsorbed in a surface interstice (Figure 4A_1). Then another proton (H^+) gets close to the adsorbed proton (H_{ad}) (Figure 4A_2) to form an adsorbed H_2. After migrating to a metal site (Figure 4A_3), the absorbed H_2 finally makes its way to desorption. Note that while the product H_2 is formed on the Ni site on the surface of the NiS catalyst, it prefers to form on the Fe site of the INS catalyst. It thus appears that the change of electronic structure of the catalytically active center arising from the Fe-incorporation can modulate and facilitate the HER process. Importantly, the fluent product migration rapidly vacates the active site for the next HER turnover cycle, promoting the overall catalytic activity. Therefore, our INS catalysts work in a metal–ligand cooperative catalysis mode, similar to that of metal complex catalysts and hydrogenases toward HER. For a metal complex catalyst, it incorporates proton that relays from pendant acid–base groups that position close to the metal center where hydrogen production occurs,[18] and the active sites of hydrogenase feature pendant base proximate to the metal centers as well.[19] In our case, with pendant bases S close to the metal centers of Fe and Ni, the INS nanosheets have a similar structure and chemical composition to those of $NiFeS_2$(μ-H) core in the active site of [NiFe]-H_2ase hydrogenase and NiFe thiolato hydride complex.[18a,20] Therefore, it is reasonable that the INS ultrathin nanosheets might share a similar catalytic mechanism to the metal complex catalysts and hydrogenases toward the HER.

In general, the activity of an HER catalyst is related to the kinetic barrier of the rate-determining H_2 evolution pathway. To shed more light on the Fe-enhanced catalytic activity, we further investigated the energy profiles along the HER pathway on α-INS and α-NiS slabs by DFT (Figure 4B). As mentioned above, the rate-determining step is thought to be the combination of H_{ad} with H^+. Significantly, the energy barrier

DOI: 10.1021/jacs.5b07728
J. Am. Chem. Soc. 2015, 137, 11900–11903

for this step is calculated to be only 0.01 eV on the α-INS slab, which is much lower than that on NiS (0.19 eV). Moreover, the released energy for the formation of H_2 on α-INS slab is 2.39 eV, which is also advantageously larger than that on NiS slab (2.19 eV). Therefore, drawing on the simulation results, the higher catalytic activity of the INS nanosheets than the pristine NiS nanosheets on HER in acidic solution is attributed to the lower energy barrier for H^+ adsorption and the higher exothermicity for H_2 formation. For comparison, the HER pathways on β-INS and β-NiS catalysts were also investigated (Figure S13), which also accord well with the experimental results.

In summary, β-INS ultrathin nanosheets have been successfully synthesized by topotactic sulfidation of FeNi LDH precursors and proved to be excellent HER catalysts in strong acidic solutions. What is more, metallic α-INS ultrathin nanosheets obtained by annealing treatment of the β-INS show further improved HER performance with a low overpotential of 105 mV for 10 mA/cm^2, a small Tafel slope of 40 mV/dec, and long time stability. Some important features of the ultrathin HER catalyst are believed to have played a key role: (1) the rich and accessible catalytic active sites, (2) the felicitous electronic environments of the bitransition metal system that enhance HER catalytic activity and durability, and (3) the intrinsic metallic character of α-INS, which further hastens charge transfer and forestalls any possible overpotential from Schottky barriers. Our DFT calculations have shown that the suitable kinetics and energetics for the H^+ adsorption and H_2 formation contribute to the advanced HER catalytic activity. To our knowledge, this is the first study on multitransition metal based sulfide nanosheets with atomic thickness as HER catalysts with a remarkable electrocatalytic performance, opening up an exciting avenue to expand the family of low cost HER catalysts with high activity and long-term stability.

■ ASSOCIATED CONTENT

Supporting Information

The Supporting Information is available free of charge on the ACS Publications website at DOI: 10.1021/jacs.5b07728.

Experimental procedures and supporting data including SEM, TEM, HRTEM, AFM, and EDX of catalysts (PDF)

■ AUTHOR INFORMATION

Corresponding Author

*chsyang@ust.hk

Notes

The authors declare no competing financial interest.

■ ACKNOWLEDGMENTS

This work was supported by the NSFC/RGC Joint Research Scheme (Grant N_HKUST610/14).

■ REFERENCES

(1) (a) Dresselhaus, M.; Thomas, I. *Nature* **2001**, *414*, 332. (b) Cook, T. R.; Dogutan, D. K.; Reece, S. Y.; Surendranath, Y.; Teets, T. S.; Nocera, D. G. *Chem. Rev.* **2010**, *110*, 6474.

(2) Dasgupta, N. P.; Liu, C.; Andrews, S.; Prinz, F. B.; Yang, P. *J. Am. Chem. Soc.* **2013**, *135*, 12932.

(3) (a) Liang, H.; Li, L.; Meng, F.; Dang, L.; Zhuo, J.; Forticaux, A.; Wang, Z.; Jin, S. *Chem. Mater.* **2015**, *27*, 5702. (b) Voiry, D.; Yamaguchi, H.; Li, J.; Silva, R.; Alves, D. C.; Fujita, T.; Chen, M.; Asefa, T.; Shenoy, V. B.; Eda, G.; Chhowalla, M. *Nat. Mater.* **2013**, *12*, 850. (c) Wang, H.; Lu, Z.; Kong, D.; Sun, J.; Hymel, T. M.; Cui, Y. *ACS Nano* **2014**, *8*, 4940. (d) Jaramillo, T. F.; Jørgensen, K. P.; Bonde, J.; Nielsen, J. H.; Horch, S.; Chorkendorff, I. *Science* **2007**, *317*, 100. (e) Hinnemann, B.; Moses, P. G.; Bonde, J.; Jørgensen, K. P.; Nielsen, J. H.; Horch, S.; Chorkendorff, I.; Nørskov, J. K. *J. Am. Chem. Soc.* **2005**, *127*, 5308. (f) Lukowski, M. A.; Daniel, A. S.; English, C. R.; Meng, F.; Forticaux, A.; Hamers, R.; Jin, S. *Energy Environ. Sci.* **2014**, *7*, 2608.

(4) (a) Yang, J.; Duan, X.; Qin, Q.; Zheng, W. *J. Mater. Chem. A* **2013**, *1*, 7880. (b) Hou, L.; Yuan, C.; Li, D.; Yang, L.; Shen, L.; Zhang, F.; Zhang, X. *Electrochim. Acta* **2011**, *56*, 7454. (c) Ni, S.; Yang, X.; Li, T. *J. Mater. Chem.* **2012**, *22*, 2395. (d) Sun, H.; Qin, D.; Huang, S.; Guo, X.; Li, D.; Luo, Y.; Meng, Q. *Energy Environ. Sci.* **2011**, *4*, 2630.

(5) (a) Trotochaud, L.; Young, S. L.; Ranney, J. K.; Boettcher, S. W. *J. Am. Chem. Soc.* **2014**, *136*, 6744. (b) Hunter, B. M.; Blakemore, J. D.; Deimund, M.; Gray, H. B.; Winkler, J. R.; Müller, A. M. *J. Am. Chem. Soc.* **2014**, *136*, 13118. (c) Smith, A. M.; Trotochaud, L.; Burke, M. S.; Boettcher, S. W. *Chem. Commun.* **2015**, *51*, 5261.

(6) (a) Cheng, L.; Huang, W.; Gong, Q.; Liu, C.; Liu, Z.; Li, Y.; Dai, H. *Angew. Chem., Int. Ed.* **2014**, *53*, 7860. (b) Lin, J.; Peng, Z.; Wang, G.; Zakhidov, D.; Larios, E.; Yacaman, M. J.; Tour, J. M. *Adv. Energy Mater.* **2014**, *4*, 1301875. (c) Lukowski, M. A.; Daniel, A. S.; Meng, F.; Forticaux, A.; Li, L.; Jin, S. *J. Am. Chem. Soc.* **2013**, *135*, 10274. (d) Xie, J.; Zhang, H.; Li, S.; Wang, R.; Sun, X.; Zhou, M.; Zhou, J.; Lou, X. W. D.; Xie, Y. *Adv. Mater.* **2013**, *25*, 5807.

(7) (a) Long, X.; Li, J.; Xiao, S.; Yan, K.; Wang, Z.; Chen, H.; Yang, S. *Angew. Chem.* **2014**, *126*, 7714. (b) Long, X.; Xiao, S.; Wang, Z.; Zheng, X.; Yang, S. *Chem. Commun.* **2015**, *51*, 1120.

(8) Gong, M.; Li, Y.; Wang, H.; Liang, Y.; Wu, J. Z.; Zhou, J.; Wang, J.; Regier, T.; Wei, F.; Dai, H. *J. Am. Chem. Soc.* **2013**, *135*, 8452.

(9) (a) Huang, L.; Chen, D.; Ding, Y.; Wang, Z. L.; Zeng, Z.; Liu, M. *ACS Appl. Mater. Interfaces* **2013**, *5*, 11159. (b) Yuan, C.; Li, J.; Hou, L.; Zhang, X.; Shen, L.; Lou, X. W. D. *Adv. Funct. Mater.* **2012**, *22*, 4592.

(10) Thomas, J. E.; Skinner, W. M.; Smart, R. S. *Geochim. Cosmochim. Acta* **2003**, *67*, 831.

(11) (a) Cao, B.; Veith, G. M.; Neuefeind, J. C.; Adzic, R. R.; Khalifah, P. G. *J. Am. Chem. Soc.* **2013**, *135*, 19186. (b) Kong, D.; Wang, H.; Lu, Z.; Cui, Y. *J. Am. Chem. Soc.* **2014**, *136*, 4897.

(12) Zhao, Z.; Wu, H.; He, H.; Xu, X.; Jin, Y. *Adv. Funct. Mater.* **2014**, *24*, 4698.

(13) (a) Liu, Q.; Jin, J.; Zhang, J. *ACS Appl. Mater. Interfaces* **2013**, *5*, 5002. (c) Wang, D.-Y.; Gong, M.; Chou, G.-L.; Pan, C.-J.; Chen, H.-A.; Wu, Y.; Lin, M.-C.; Guan, M.; Yang, J.; Chen, C.-W.; Wang, Y.-L.; Hwang, B.-J.; Chen, C.-C.; Dai, H. *J. Am. Chem. Soc.* **2015**, *137*, 1587.

(14) Merki, D.; Vrubel, H.; Rovelli, L.; Fierro, S.; Hu, X. *Chem. Sci.* **2012**, *3*, 2515.

(15) (a) Xu, K.; Chen, P.; Li, X.; Tong, Y.; Ding, H.; Wu, X.; Chu, W.; Peng, Z.; Wu, C.; Xie, Y. *J. Am. Chem. Soc.* **2015**, *137*, 4119. (b) Faber, M. S.; Dziedzic, R.; Lukowski, M. A.; Kaiser, N. S.; Ding, Q.; Jin, S. *J. Am. Chem. Soc.* **2014**, *136*, 10053.

(16) (a) Tian, J.; Liu, Q.; Asiri, A. M.; Sun, X. *J. Am. Chem. Soc.* **2014**, *136*, 7587. (b) Popczun, E. J.; McKone, J. R.; Read, C. G.; Biacchi, A. J.; Wiltrout, A. M.; Lewis, N. S.; Schaak, R. E. *J. Am. Chem. Soc.* **2013**, *135*, 9267.

(17) Conway, B.; Tilak, B. *Electrochim. Acta* **2002**, *47*, 3571.

(18) (a) Barton, B. E.; Rauchfuss, T. B. *J. Am. Chem. Soc.* **2010**, *132*, 14877. (b) Wilson, A. D.; Shoemaker, R.; Miedaner, A.; Muckerman, J.; DuBois, D. L.; DuBois, M. R. *Proc. Natl. Acad. Sci. U. S. A.* **2007**, *104*, 6951.

(19) Nicolet, Y.; de Lacey, A. L.; Vernede, X.; Fernandez, V. M.; Hatchikian, E. C.; Fontecilla-Camps, J. C. *J. Am. Chem. Soc.* **2001**, *123*, 1596.

(20) Barton, B. E.; Whaley, C. M.; Rauchfuss, T. B.; Gray, D. L. *J. Am. Chem. Soc.* **2009**, *131*, 6942.

DOI: 10.1021/jacs.5b07728
J. Am. Chem. Soc. 2015, 137, 11900−11903